Received: 23 December 2022 | Revised: 4 April 2023 | Accepted: 19 April 2023 | Published on: 8 May 2023

DOI: 10.1002/mrm.29696

TECHNICAL NOTE

Magnetic Resonance in Medicine

Deuterium echo-planar spectroscopic imaging (EPSI) in the human liver in vivo at 7 T

Kyung Min Nam | **Ayhan Gursan** | **Alex A. Bhogal** | **Jannie P. Wijnen** | **Dennis W. J. Klomp** | **Jeanine J. Prompers** | **Arjan D. Hendriks**

Center for Image Sciences, Department of High Field MR Research, University Medical Center Utrecht, Utrecht, the Netherlands

Correspondence
Kyung Min Nam, University Medical Center Utrecht, Department of High Field MR Research, Room Q02.2.210, Heidelberglaan 100 (PO BOX 85500), 3584 CX Utrecht, the Netherlands.
Email: k.m.nam@umcutrecht.nl

Funding information
European Union's, Marie Sklodowska-Curie, Grant/Award Number: 813120; High Tech Systems and Materials (HTSM) grant from Dutch Research Council (NWO) - Toegepaste en Technische Wetenschappen (TTW), Grant/Award Number: 17134; Future and Emerging Technologies (FET) Innovation Launchpad grant from the EU, Grant/Award Number: 850488

Purpose: To demonstrate the feasibility of deuterium echo-planar spectroscopic imaging (EPSI) to accelerate 3D deuterium metabolic imaging in the human liver at 7 T.

Methods: A deuterium EPSI sequence, featuring a Hamming-weighted k-space acquisition pattern for the phase-encoding directions, was implemented. Three-dimensional deuterium EPSI and conventional MRSI were performed on a water/acetone phantom and in vivo in the human liver at natural abundance. Moreover, in vivo deuterium EPSI measurements were acquired after oral administration of deuterated glucose. The effect of acquisition time on SNR was evaluated by retrospectively reducing the number of averages.

Results: The SNR of natural abundance deuterated water signal in deuterium EPSI was 6.5% and 5.9% lower than that of MRSI in the phantom and in vivo experiments, respectively. In return, the acquisition time of in vivo EPSI data could be reduced retrospectively to 2 min, beyond the minimal acquisition time of conventional MRSI (of 20 min in this case), while still leaving sufficient SNR. Three-dimensional deuterium EPSI, after administration of deuterated glucose, enabled monitoring of hepatic glucose dynamics with full liver coverage, a spatial resolution of 20 mm isotropic, and a temporal resolution of 9 min 50 s, which could retrospectively be shortened to 2 min.

Conclusion: In this work, we demonstrate the feasibility of accelerated 3D deuterium metabolic imaging of the human liver using deuterium EPSI. The acceleration obtained with EPSI can be used to increase temporal and/or spatial resolution, which will be valuable to study tissue metabolism of deuterated compounds over time.

KEYWORDS
deuterium MRSI, EPSI, hamming weighted MRSI, liver, glucose dynamics, 7 T

Preliminary results of this work have recently been presented at the annual meeting of the ISMRM 2021, as oral presentation (#0231, https://cds.ismrm.org/protected/21MPresentations/abstracts/0231.html).

1 | INTRODUCTION

Perturbations in energy metabolism are common in many diseases, including cancer, neurodegenerative diseases, diabetes, and nonalcoholic fatty liver disease.[1–3] Deuterium metabolic imaging (DMI)[4] is an emerging metabolic imaging technique based on deuterium MRSI in combination with the intake of deuterium-labeled substrates, such as [6,6′-$^2H_2$]-glucose. It has been demonstrated that DMI can be used to detect differences in glucose metabolism in tumor (e.g., the Warburg effect[5,6]) and healthy brain tissue in vivo by measuring the production of deuterated lactate and deuterated glutamate and glutamine in a 3D spatially resolved manner.[4] DMI also has the potential to measure glucose metabolism in other tissues, such as the liver,[4,7] which plays an important role in maintaining whole-body glucose homeostasis.

DMI measurements obtained with conventional MRSI (i.e., phased-encoded MRSI) sequences sample the signal points of the time domain in every individual k-space location consecutively, which is time-consuming, especially for measurements with extensive 3D coverage. This limits the spatial and/or temporal resolution and prohibits finer scale evaluation of kinetics. To be able to determine glucose metabolic fluxes from dynamic DMI measurements, the temporal resolution should be sufficiently high. From carbon-13 (^{13}C) studies, it is known that to quantify, for example, cerebral glucose metabolism kinetics, a temporal resolution of about 5 min is required.[8] Previous methods address this challenge by using nonlocalized deuterium MRS sequences[9,10] or by sacrificing spatial resolution in favor of shorter acquisition times.[7,11–19]

Similar to MRSI based on nuclei such as proton,[20–23] phosphorus (^{31}P)[24–26] and carbon (^{13}C),[27–29] the use of an echo-planar readout is an attractive method to accelerate DMI.[30] Echo-planar spectroscopic imaging (EPSI) acquires samples in the presence of a rapidly oscillating readout gradient, and thus enables the encoding of time signal points from several k-space locations in a row per TR. However, a drawback of EPSI is the limited achievable spectral bandwidth for a single shot, particularly at high magnetic field strength. Unlike the more complex proton MR spectrum, only a few signals (i.e., water, lipids, glucose, glutamate and glutamine, and lactate) are visible in the deuterium spectrum between 1 and 5 ppm (183-Hz bandwidth) at 7 T after administration of deuterated glucose. Therefore, the EPSI readout could be particularly suited for application in deuterium studies.

Nevertheless, the reduced scan time and/or increased spatial resolution that can be obtained with an EPSI readout comes at the cost of a lower SNR per unit time and unit volume.[31] The main factors influencing the SNR efficiency during the readout are gradient hardware limitations and whether samples are acquired during the ramp phases of the gradient lobes.[24,25,31] The use of ultrahigh field (≥7 T) holds significant potential to alleviate the SNR constraints for EPSI, as the sensitivity of DMI was shown to scale supralinearly with field strength, resulting in a fourfold higher sensitivity at 7 T than at 3 T.[32] For ^{1}H-MRI/MRS, challenges arise at higher field strengths, such as artifacts caused by increased B_0 and B_1^+ field inhomogeneities, and increased specific absorption rates. However, because the Larmor frequency of deuterium is much lower than that of proton, B_1^+ fields in deuterium are more homogeneous, and specific absorption rate is also much lower in DMI compared with ^{1}H MRI/MRS, as there is no need for water and lipid suppression pulses or decoupling. The B_0 inhomogeneities are still present but have less influence on the deuterium spectral quality due to the large intrinsic line widths of the signals of the quadrupolar deuterium nuclei.[33]

This study aims to demonstrate the feasibility of deuterium EPSI to increase the spatial and temporal resolution for body applications to facilitate metabolic measurements at 7 T, specifically for the human liver. For more efficient spatial sampling, the EPSI sequence was combined with a Hamming-weighted acquisition. Deuterium EPSI and conventional MRSI were performed on a water/acetone phantom and in vivo. Deuterium EPSI and MRSI were compared in terms of SNR at the same temporal resolution. Additionally, the possible gain in temporal resolution of EPSI was investigated beyond the minimal scan time for MRSI by reducing the number of signal averages.

2 | METHODS

2.1 | Experimental setup

All experiments were performed using a 7T MR scanner (Philips Medical Systems, Best, the Netherlands) equipped with a ^{1}H/^{2}H transmit-receive body array.[34] Before each MRSI/EPSI scan, ^{1}H B_0 maps were acquired for second-order image-based B_0 shimming,[35] and anatomical ^{1}H T_1-weighted and Dixon images were acquired to plan deuterium MRSI and EPSI scans. Deuterium-labeled glucose (i.e., [6–6′-$^2H_2$]glucose) was purchased from Buchem B.V. (Apeldoorn, the Netherlands).

2.2 | Hamming-weighted acquisition scheme

For a more efficient spatial sampling, the EPSI sequence was combined with acquisition weighting[26,36,37] (Figure 1)

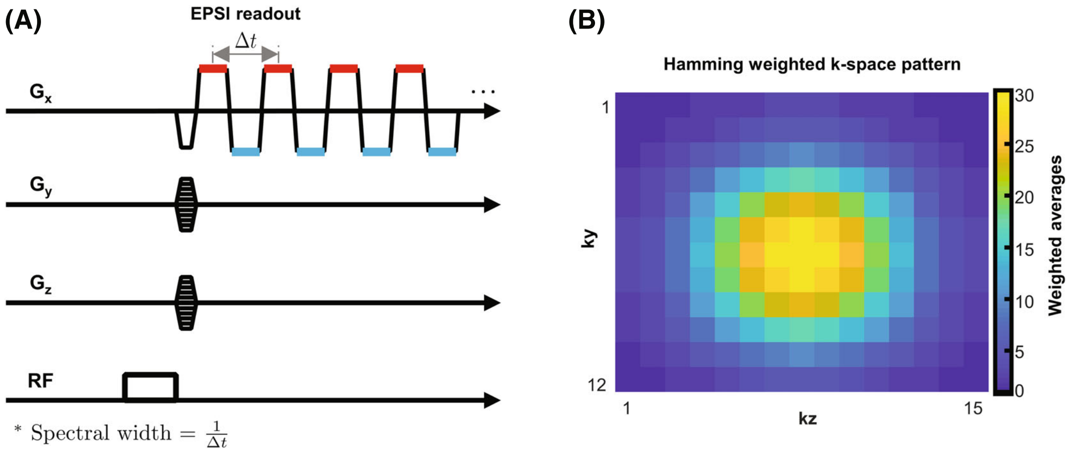

FIGURE 1 (A) Illustration of the deuterium echo-planar spectroscopic imaging (EPSI) pulse sequence. An oscillating trapezoidal readout gradient (G_x) with a period of Δt was used to induce a train of gradient echoes. Data samples were collected on the gradient plateaus of both odd (red) and even (blue) numbered gradients. (B) A Hamming-weighted acquisition pattern was applied in the two phase-encoding directions to increase SNR per unit of time. The shown example is from the in vivo data sets acquired after intake of deuterated glucose (Figures 3–5).

in the two phase-encoding directions according to

$$WNSA\left(k_y, k_z\right) = NSA \cdot W\left(k_y, k_z\right) \tag{1}$$

with the number of signal averages (NSA) and the Hamming-weighting function:

$$W\left(r\left(k_y, k_z\right)\right) = 0.54 + 0.46\cos(\pi \cdot r), \tag{2}$$

where r is the radial distance[26] of $\left(k_y, k_z\right)$ in k-space. For the MRSI sequence, Hamming-weighted acquisition was applied in three phase-encoding directions. To correct for the difference between the 2D acquisition-weighted pattern of EPSI and the 3D acquisition-weighted pattern of MRSI, a Hamming k-space filter was applied in the readout direction (k_x) of the EPSI k-space data during postprocessing (see also Section 2.5).

2.3 | Acquisition of phantom data

For phantom experiments, a glass bottle (1 L) with 50% acetone and 50% water was used with naturally abundant deuterium levels. Deuterium EPSI and MRSI spectra were acquired using a rectangular RF excitation pulse of 1-ms duration. The scan parameters were voxel size = 20 × 20 × 20 mm^3, FOV = 200 (right–left [RL]) × 140 (anterior–posterior [AP]) × 280 (feet–head [FH]) mm^3, TR/TE = 340/1.0 ms, spectral bandwidth = 1830 Hz, and the number of time samples = 512. For EPSI alone, readout direction = RL, oversampling factor in k_x direction = 2, plateau duration of a gradient lobe = 0.3462 ms, gradient strength = 19.89 mT/m, gradient slew rate = 198.7 mT/m/ms, and readout time = 279.8 ms. Acquisition times were as follows: EPSI with 76 weighted averages (i.e., in the center of k-space, also for all following instances) = 11 min 8 s; and MRSI with 10 weighted averages = 11 min 12 s.

2.4 | Acquisition of in vivo data

The study was approved by the local medical ethics committee, and participants gave written informed consent before scanning. Deuterium MRSI and EPSI were performed on the liver of 3 healthy volunteers. Subjects were positioned supine with the ^{1}H/^{2}H coil strapped around the body, but slightly shifted to the right side for optimal liver coverage. For 2 volunteers, MRSI and EPSI scans were acquired in the liver without administration of a ^{2}H-labeled substrate. For the third volunteer, two EPSI scans were obtained in the liver at 2 h 14 min and 3 h 11 min after oral intake of deuterated glucose (50 g [6,6′-^{2}H$_2$]glucose dissolved in water). All in vivo MRSI and EPSI spectra were obtained with acquisition weighting and with the following scan parameters: voxel size = 20 × 20 × 20 mm^3, FOV = 360 (RL) × 240 (AP) × 300 (FH) mm^3, TR/TE = 371/1.0 ms, 512 time samples, and spectral bandwidth = 721.5 Hz for EPSI and 1443 Hz for MRSI. For EPSI alone, readout direction = RL, readout oversampling factor = 4, plateau duration of a gradient lob = 0.5667 ms, gradient strength = 12.75 mT/m, gradient slew rate = 200 mT/m/ms, and readout time = 354.81 ms. Acquisition times for the measurements at natural abundance were as follows: EPSI with 82 weighted averages was 25 min 48 s; and MRSI with four weighted averages was 25 min 56 s. The acquisition time for the EPSI scans after oral intake of deuterated glucose was 9 min 50 s with 30 weighted averages. Experiments were performed without respiratory gating.

2.5 | Data reconstruction and processing

MRSI and EPSI data were processed offline using in-house-developed scripts written in *MATLAB* (MathWorks, Natick, Massachusetts, USA). For the EPSI data set, first the superfluous data acquired in the oversampled readout direction (k_x) was removed in image domain. Next, the average signal was calculated (over the NSA) in k-space, and odd echo lines were flipped. A first-order phase correction[25,26] was performed, taking into account the different time delays (i.e., $\Delta t(k_x)/2$) of the samples relative to the RF pulse. The EPSI data from odd/even echoes were processed separately to avoid Nyquist ghosting artifacts.[38] Zero-filling to 512 sample points was performed in time domain. A Hamming k-space filter was applied only in the readout direction of the EPSI data during postprocessing. This procedure transformed the 2D acquisition-weighted pattern into a 3D weighted pattern for EPSI, for better comparison with the 3D acquisition-weighted MRSI. Next, an additional correction on the Hamming-weighting coefficients was applied in all k-space directions for MRSI and DEPSI acquisitions, to better match the discrete number of acquired averages (staircase acquisition pattern) with the ideal Hamming function (smooth pattern). After a zero-order phase correction, the EPSI data were combined from separated echoes. For the MRSI data sets, the reconstruction and postprocessing steps were performed as similarly as possible to the EPSI procedures for a fair comparison.

Before the channel combination, the noise matrix (Ψ) was calculated.[23] To acquire sufficient noise samples (η) ($\geq$20,000) for each receiver channel, a separate noise scan was performed. After the spatial Fourier transform, the Roemer equal noise algorithm[39–41] was used for channel combination. The sensitivities S were obtained from the average of the first four sample points in the FID signal.[42,43] Next, frequency alignment of the individual spectra was performed. A principal component analysis–based (PCA) denoising[44] method was implemented to remove noise from deuterium EPSI spectra after administering deuterated glucose, but all other data were not denoised.

Retrospective removal of k-space averages was performed to evaluate the spectral quality for different scan times. At the start of the reconstruction procedure, the number of k-space averages was incrementally decreased retrospectively while maintaining a Hamming-weighted k-space pattern.

2.6 | Quantification

The SNR was calculated in the spectral domain according to $SNR = I_{water}/\sigma(I_{Noise})$, with I_{water} being the water signal intensity, and $\sigma(I_{Noise})$ being the SD of noise between 8 and 12 ppm. In the EPSI spectra recorded after deuterated glucose intake, deuterated water and glucose signals were fit using the AMARES (advanced method for accurate, robust, and efficient spectral fitting) algorithm[45] implemented in the OXSA toolbox.[46] Deuterated glucose/water maps were then calculated from the fitted amplitudes, where the water amplitudes were used from the second scan. T_1 relaxation corrections were not considered. The full width at half maximum (FWHM) obtained from the AMARES fits was used to calculate T_2* relaxation times according to $1/(\pi \cdot \mathrm{FWHM})$, under the assumption of Lorentzian line shapes.

3 | RESULTS

3.1 | Phantom results

For the phantom measurements, naturally abundant deuterium signals from water and acetone were observed for both Hamming-weighted 3D deuterium EPSI and MRSI acquisitions with similar peak ratios (Figure 2A,C). The average SNR of the water peak was calculated for 18 selected voxels in the three middle slices for the full acquisitions and after incrementally decreasing the NSA (Figure 2B). For both acquisition methods, the SNR decreased with decreasing total acquisition time. For long acquisitions of approximately 11 min, the SNR of the weighted MRSI measurement (64.4 ± 23.6) appeared to be higher than the SNR of the weighted EPSI measurement (60.2 ± 15.0). Both peaks were resolved at all locations, and the ratio of acetone to water was similar for deuterium EPSI and MRSI (Figure 2C). For the EPSI acquisition, the scan time could be reduced to 2 min, while still being able to distinguish both the water and acetone peaks (Figure 2D). For the MRSI method, this reduction in scan time could not be achieved; when keeping the FOV, voxel size and TR constant, the minimum scan time for fully sampled MRSI was 5 min 39 s for one NSA.

3.2 | In vivo results

Signals from naturally abundant deuterated water in the liver were detected in both 3D MRSI and EPSI data with 20-mm (nominal) isotropic voxels (Figure 3 and Figure S1). Spectral quality in terms of SNR was comparable for the 25 min 56 s MRSI (4 weighted averages)

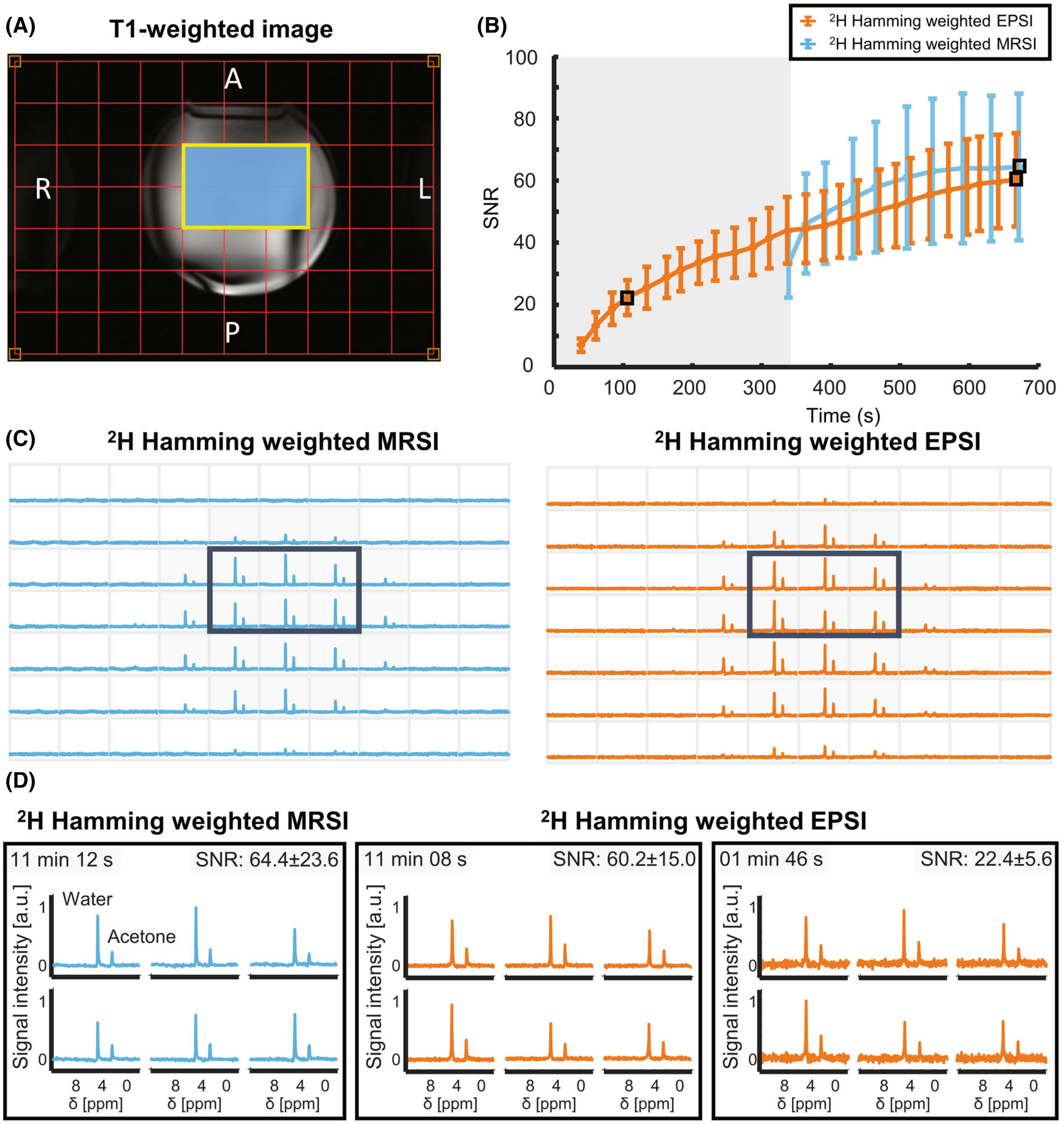

FIGURE 2 A phantom with water (50%) and acetone (50%) without deuterium enrichment was scanned with 3D EPSI and 3D MRSI acquisitions. (A) ^{1}H T$_1$-weighted MR image of the phantom overlaid with a region of interest (ROI) that includes six voxels in the middle slice. (B) Average SNR of the water peak using two different acquisition methods: Hamming-weighted EPSI (orange line) and Hamming-weighted MRSI (blue line). The SNR as a function of acquisition time calculated by changing the number of weighted averages from 76 to 1 in steps of 3 for EPSI and 10 to 1 in steps of 1 for MRSI, retrospectively. The SNR was calculated for 18 selected voxels (A, blue region) in the three middle slices. With the MRSI method, it was not possible to acquire data in less than 5 min 39 s, when keeping the FOV, resolution, and TR constant (B, gray region). (C) Deuterium spectra of the middle slice are shown for both MRSI (blue) and EPSI (orange) with a Hamming-weighted acquisition. (D) Deuterium spectra of the ROI are shown for both Hamming-weighted EPSI (orange) and MRSI (blue) acquisitions. The water and acetone peaks can be detected in both acquisitions with equal acquisition time. Note that both the water and acetone peaks can be detected with deuterium EPSI in less than 2 min (10 weighted averages). Measurement parameters: full k-space sampling, nominal voxel size $V_{nom} = 8$ mL, zero-filling to 512 points, no denoising, no line broadening, and no baseline correction.

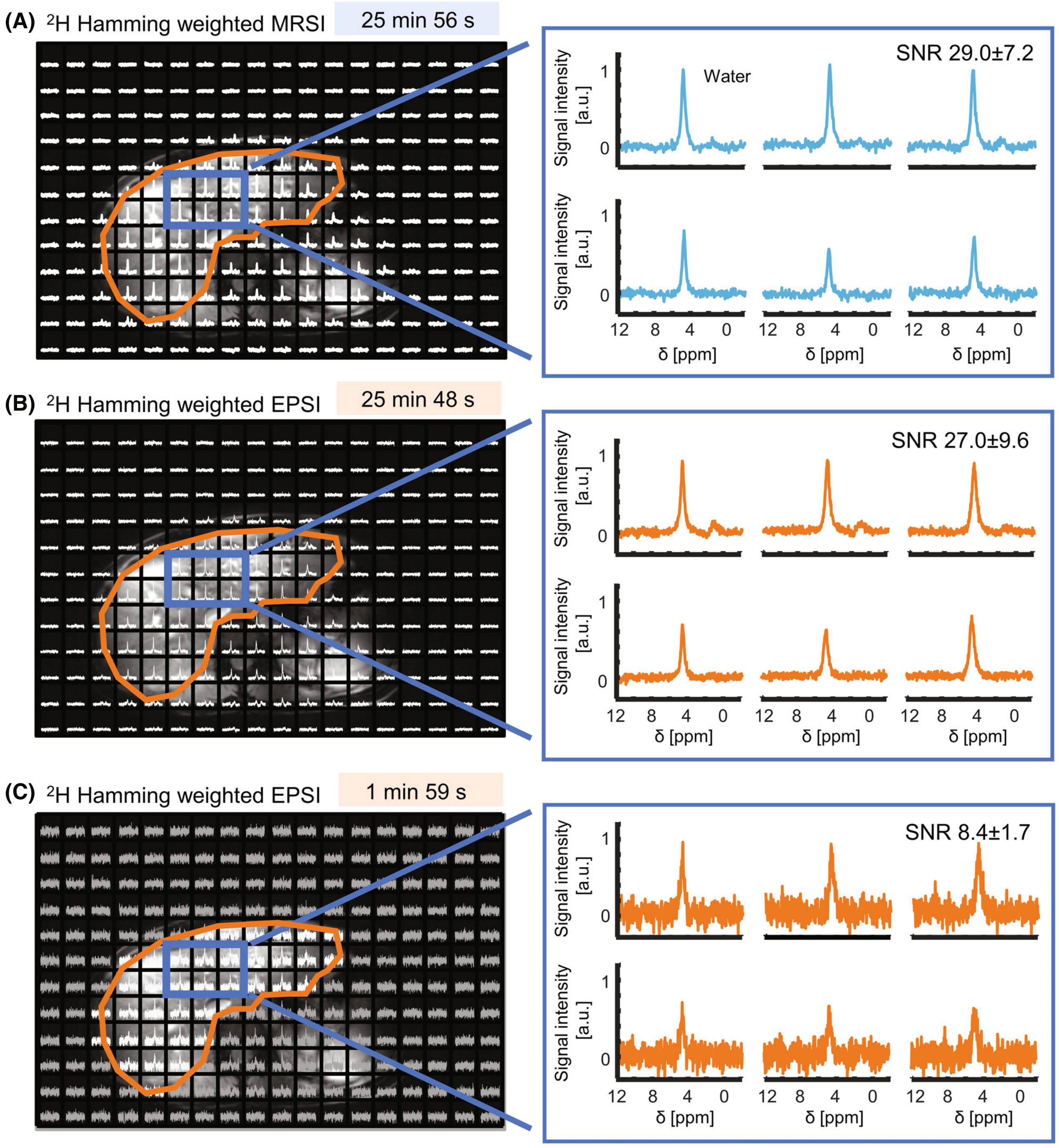

FIGURE 3 Three-dimensional data sets of the human liver at natural abundance, acquired with both Hamming-weighted MRSI (A) and EPSI acquisitions (B,C). The left panels show overlays of the ^{1}H-MRI images (Dixon) and the ^{2}H spectra. The liver is contoured in orange in the left panels. The right panels highlight the selected six voxels located in the liver (left panels, blue box), and SNR was calculated for 18 voxels from the three middle slices. Measurement parameters: nominal voxel size $V_{nom} = 8$ mL, zero-filling to 512 points, baseline correction was applied, but no line broadening and no denoising.

and 25 min 48 s EPSI (82 weighted averages) acquisitions (SNR = 29.0 ± 7.2 vs. 27.0 ± 9.6 for the first subject, and 20.3 ± 3.9 vs. 19.3 ± 3.7 for the second subject; Table S1). For EPSI, the scan time could be reduced to 2 min (four weighted averages), while still being able to detect the deuterated water peak.

The 3D-EPSI data with 20-mm isotropic voxels acquired 2 h 14 min after oral intake of [6,6'-$^2H_2$]glucose showed resonances of deuterated water and glucose in the liver (Figure 4). The average SNR of the deuterated water signals decreased with retrospectively reduced acquisition times (Figure 4B). EPSI could still detect both deuterated

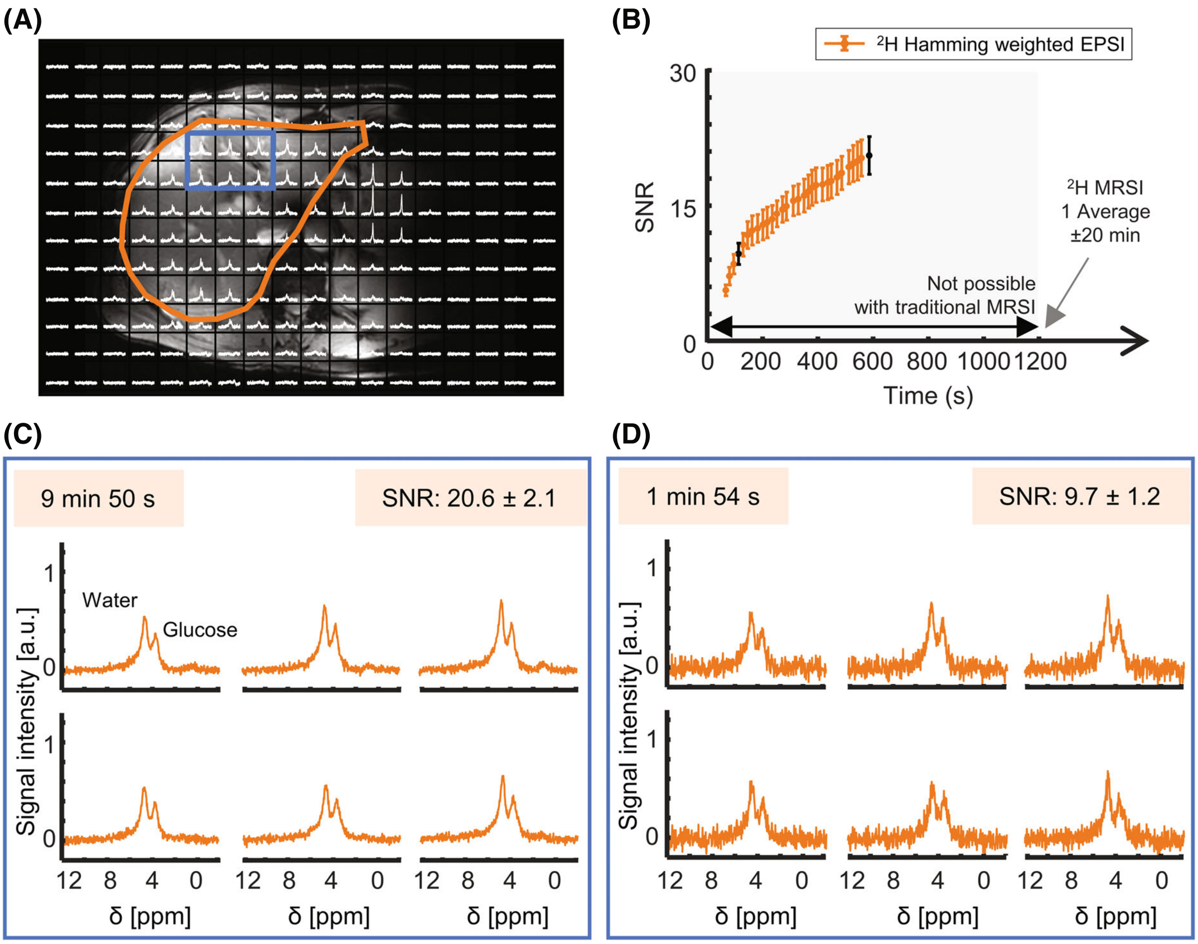

FIGURE 4 Three-dimensional data sets of the human liver after intake of deuterated glucose, acquired with the Hamming-weighted EPSI acquisition (2 h 14 min after oral [6,6′-$^2H_2$]glucose intake). (A) Overlays of the ^{1}H-MRI images (Dixon) and the ^{2}H spectra. The liver contour is highlighted in orange. The selected voxels in the liver (A, blue box) show the water and glucose peak. The average SNR of the deuterated water signal in the ROI (A, blue box) was calculated from 18 voxels in the three middle slices of the liver. The SNR as a function of acquisition time (B) was estimated by decreasing the number of weighted averages retrospectively from 30 to 1 in steps of 1. Two acquisition times (B, black points) are selected, from which deuterium EPSI spectra are displayed (C, 30 weighted averages; D, 4 weighted averages). With full liver coverage and the same resolution, a conventional MRSI scan would take at least 20 min for one average to acquire (B, red arrow).

water and glucose signals when shortening the acquisition time from 9 min 50 s to 1 min and 54 s (Figure 4D). In contrast, fully sampled MRSI with the same FOV, voxel size, TR, and one NSA would require a minimum scan time of about 20 min. The mean FWHM of the deuterated water and glucose signals was 24.7 ± 2.2 Hz and 34.6 ± 4.6 Hz, respectively, in the 18 selected voxels in three slices in the liver (Figure 4), corresponding to T_2* relaxation times of 13.0 ± 1.1 ms for deuterated water 9.6 ± 1.3 ms for deuterated glucose.

Figure 5A shows the same in vivo deuterium EPSI data as Figure 4 (2 h 14 min after intake of [6,6′-$^2H_2$]glucose), but now with PCA denoising for visualization. Furthermore, a data set acquired approximately 1 h later in the same subject at 3 h 11 min after intake is shown (Figure 5B). The deuterated glucose signal in the liver decreased between these two time points, whereas the deuterated water signal increased. In the glucose/water metabolic ratio maps calculated from the two EPSI scans (Figure 5C,D), a high glucose/water ratio was observed in the stomach in the first EPSI scan, which had disappeared during the second scan.

4 | DISCUSSION

In this work, we implemented a 3D deuterium MRSI sequence that combines an EPSI readout[24–26,28,47] with a Hamming-weighted acquisition. This EPSI sequence was designed to accelerate the acquisition of deuterium MRSI data in the human liver at 7 T. Deuterium EPSI measurements were successfully performed in a phantom, and in the liver in vivo at natural abundance deuterium levels, and after deuterated glucose intake. Three-dimensional

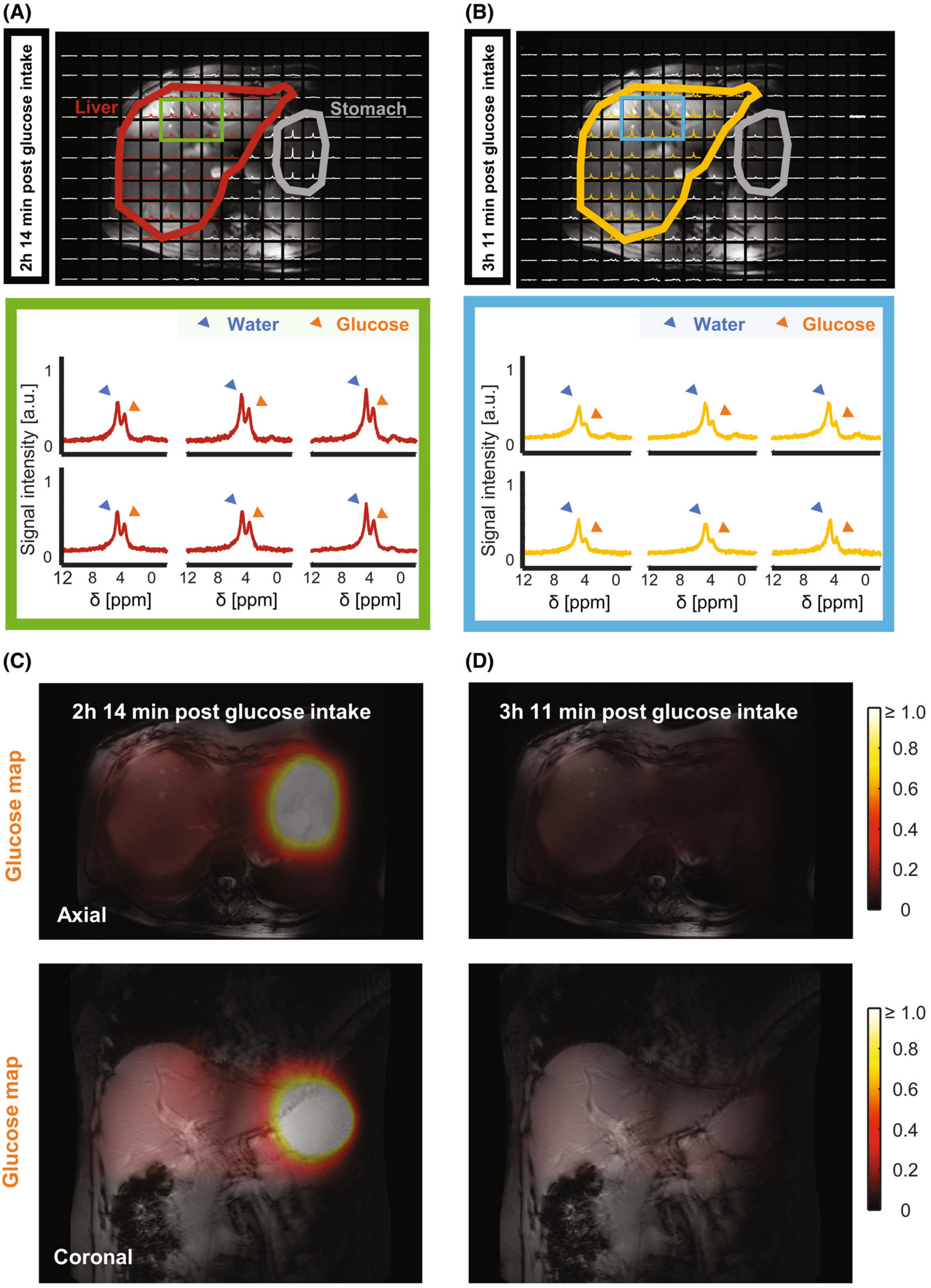

FIGURE 5 Three-dimensional EPSI scans of the liver, acquired 2 h 14 min (A) and 3 h 11 min (B), respectively, after oral [6,6′-$^2H_2$]glucose intake. In the MRI–deuterium metabolic imaging overlays (top, A and B), the liver and the stomach contours are highlighted. Selected voxels in the liver (green and blue box) show both the glucose peak (orange marker) and the water peak (blue marker). The glucose peak appears to decrease over time. Note that the glucose signal in the stomach (contoured gray) can also be detected and is much higher 2 h after intake (A) than 3 h after intake (B). For better visualization, the principal component analysis denoising method was applied (bottom, A and B). Metabolic maps (C,D) were defined by the ratio between the glucose and water signal of two time points in the transverse (top) and coronal plane (bottom). Glucose/water ratio maps of the deuterium EPSI data (C,D) after oral [6,6′-$^2H_2$]glucose intake are overlaid with the anatomical images. The maps show the glucose/water ratio 2 h (C) and 3 h (D) after oral intake.

EPSI scans after administering deuterated glucose enabled monitoring of hepatic glucose dynamics with full liver coverage with a spatial resolution of 20 mm isotropic and a temporal resolution of 9 min 50 s, which could be retrospectively reduced to 1 min 54 s.

Phantom measurements resulted in high-quality spectra for both EPSI and MRSI acquisitions. The EPSI acquisition time could be reduced by a factor of 6.3 (i.e., from 11 min 08 s to 1 min 46 s), whereas MRSI (using the same parameters) required a minimum scan time of 5 min 39 s. For the in vivo measurements after administering deuterated glucose, the EPSI acquisition time was under 10 min, but could be retrospectively further reduced to 2 min, while still providing sufficient SNR to differentiate the deuterated water and glucose signals from noise ($\mathrm{SNR}_{\mathrm{water}} > 9$). In comparison, for the same parameters as the EPSI scan, the MRSI scan with full liver coverage and one NSA would take at least 20 min. Therefore, the high temporal resolution achievable with EPSI could make it a suitable choice for tracking dynamic metabolic processes in tissues.

When the spatial resolution and scan time were fixed for both sequences, the SNR of the natural abundance–deuterated water signal in EPSI was 6.5% and 6.9% lower than that of MRSI in the phantom and in vivo experiments, respectively. In other words, EPSI yields a lower sensitivity per unit of time and volume compared with conventional MRSI.[48] It is known that the lack of data sampling during the gradient ramps of the EPSI readout reduces its SNR efficiency.[31] The SNR could be improved by sampling the gradient ramps during the readout[49] followed by using gridding reconstruction methods.

The acceleration provided by EPSI could be used for measurements with a higher spatial resolution within a reasonable acquisition time, particularly useful to track slower metabolic fluctuations with high spatial detail. However, a limitation of EPSI is that the rapidly switching readout gradients produce high acoustic-noise pressure levels (≥80 dB). Similar to EPI scans used for functional MRI, this sound may cause discomfort even with mandatory hearing protection measures in place. Recent developments toward an ultrasonic switching gradient system for the brain that allows for silent scanning[50,51] could fully alleviate this effect. Another downside of the rapidly switching gradients is the potential heating of the gradients (Figure S2), particularly during dynamic EPSI scans for extended time periods. In our measurements, the signal at the end of the EPSI readout (i.e., 354.81 ms) was already largely decayed. Therefore, the deuterium EPSI readout time could be shortened by reducing the number of oscillating gradient lobes, which would lower the duty cycle of the gradients. This would alleviate gradient heating if the TR is kept fixed.

Combining echo-planar type of data-acquisition schemes with spectroscopic imaging (i.e., a hybrid MRSI and EPSI pulse sequence) and advanced reconstruction algorithms (i.e., a low-rank[52,53] and subspace modeling)[52,54–59] has the potential to overcome the limitations of gradient heating and would increase the SNR. Such an approach could be adapted in our work to further increase spatial resolution and acquisition speed of 3D DMI of the human liver at 7 T.[60] Moreover, many alternatives to speed up MRSI scans[61] based on non-Cartesian spatial-spectral encoding techniques[62–66] have already been introduced for ^{1}H MRSI. Such techniques could be suitable for DMI applications that require a high temporal resolution, such as functional brain DMI. Although our research was focused on the liver, it is worth noting that deuterium EPSI has the potential to be used in other tissues, such as the brain and skeletal muscle[67] (Figures S3 and S4) to increase the spatial resolution (i.e., a large matrix size) within a limited acquisition time.

5 | CONCLUSION

This work demonstrated the feasibility of accelerated 3D DMI of the human body by implementing a deuterium EPSI sequence at 7 T. Deuterated glucose dynamics in the liver were measured in vivo with an isotropic (nominal) spatial resolution of 20 mm covering the entire liver and a temporal resolution of less than 10 min, which could be retrospectively reduced to 2 min while still providing sufficient SNR. In comparison, conventional MRSI with the same scan parameters would take 20 min for a single average. The acceleration obtained with deuterium EPSI will be valuable in studying tissue metabolism of deuterated compounds with higher temporal and/or spatial resolution.

ACKNOWLEDGMENTS

The authors thank Dimitri Welting for building the coils, Martijn Froeling for the support of the denoising method, and Arend Heerschap and Tom Scheenen for the advice and discussion at UMCN Biomedical MR Research Group. This project received funding from the European Union's Horizon 2020 research and innovation program under the Marie Sklodowska-Curie grant agreement (No. 813120) and was funded by an HTSM grant from NWO TTW (project number 17134) and by a FET Innovation Launchpad grant from the EU (No. 850488).

ORCID

Kyung Min Nam https://orcid.org/0000-0002-9185-3986
Jeanine J. Prompers https://orcid.org/0000-0002-4756-4474

Arjan D. Hendriks https://orcid.org/0000-0002-0363-2471

REFERENCES

1. Zilberter Y, Zilberter M. The vicious circle of hypometabolism in neurodegenerative diseases: ways and mechanisms of metabolic correction. *J Neurosci Res.* 2017;95:2217-2235. doi:10.1002/jnr.24064
2. Samuel VT, Shulman GI. Clinical implications of basic research nonalcoholic fatty liver disease, insulin resistance, and ceramides. *N Engl J Med.* 2019;381:1866-1869. doi:10.1056/NEJMcibr1910023
3. Mahar R, Donabedian PL, Merritt ME. HDO production from [2H7]glucose quantitatively identifies Warburg metabolism. *Sci Rep.* 2020;10:1-10. doi:10.1038/s41598-020-65839-8
4. De Feyter HM, Behar KL, Corbin ZA, et al. *Deuterium metabolic imaging (DMI) for MRI-based 3D mapping of metabolism in vivo. Sci Adv.* 2018;4:eaat7314. doi:10.1126/sciadv.aat7314
5. Warburg VO. Über den Stoffwechsel der Carcinomzelle. *Naturwissenschaften.* 1924;12:1131-1137. doi:10.1007/BF01504608
6. Koppenol WH, Bounds PL, Dang CV. Otto Warburg's contributions to current concepts of cancer metabolism. *Nat Rev Cancer.* 2011;11:325-337. doi:10.1038/nrc3038
7. De Feyter HM, Thomas MA, Behar KL, de Graaf RA. NMR visibility of deuterium-labeled liver glycogen in vivo. *Magn Reson Med.* 2021;86:62-68. doi:10.1002/mrm.28717
8. Rothman DL, de Feyter HM, de Graaf RA, Mason GF, Behar KL. 13C MRS studies of neuroenergetics and neurotransmitter cycling in humans. *NMR Biomed.* 2011;24:943-957. doi:10.1002/nbm.1772
9. Aguayo JB, McLennan IJ, Graham C, Cheng HM. Dynamic monitoring of corneal carbohydrate metabolism using high-resolution deuterium NMR spectroscopy. *Exp Eye Res.* 1988;47:337-343. doi:10.1016/0014-4835(88)90016-4
10. Lu M, Zhu XH, Zhang Y, Mateescu G, Chen W. Quantitative assessment of brain glucose metabolic rates using in vivo deuterium magnetic resonance spectroscopy. *J Cereb Blood Flow Metab.* 2017;37:3518-3530. doi:10.1177/0271678X17706444
11. Wang T, Zhu XH, Li H, et al. Noninvasive assessment of myocardial energy metabolism and dynamics using in vivo deuterium MRS imaging. *Magn Reson Med.* 2021;86:2899-2909. doi:10.1002/mrm.28914
12. Ruhm L, Avdievich N, Ziegs T, et al. Deuterium metabolic imaging in the human brain at 9.4 Tesla with high spatial and temporal resolution. *Neuroimage.* 2021;244:118639. doi:10.1016/j.neuroimage.2021.118639
13. Veltien A, van Asten J, Ravichandran N, et al. Simultaneous recording of the uptake and conversion of glucose and choline in tumors by deuterium metabolic imaging. *Cancers (Basel).* 2021;13:4034. doi:10.3390/cancers13164034
14. Kreis F, Wright AJ, Hesse F, Fala M, Hu DE, Brindle KM. Measuring tumor glycolytic flux in vivo by using fast deuterium MRI. *Radiology.* 2020;294:289-296. doi:10.1148/radiol.2019191242
15. Mahar R, Zeng H, Giacalone A, Ragavan M, Mareci TH, Merritt ME. Deuterated water imaging of the rat brain following metabolism of [2H7]glucose. *Magn Reson Med.* 2021;85:3049-3059. doi:10.1002/mrm.28700
16. Riis-Vestergaard MJ, Laustsen C, Mariager CØ, Schulte RF, Pedersen SB, Richelsen B. Glucose metabolism in brown adipose tissue determined by deuterium metabolic imaging in rats. *Int J Obes (Lond).* 2020;44:1417-1427. doi:10.1038/s41366-020-0533-7
17. Peters DC, Markovic S, Bao Q, et al. Improving deuterium metabolic imaging (DMI) signal-to-noise ratio by spectroscopic multi-echo bSSFP: a pancreatic cancer investigation. *Magn Reson Med.* 2021;86:2604-2617. doi:10.1002/mrm.28906
18. Markovic S, Roussel T, Neeman M, Frydman L. Deuterium magnetic resonance imaging and the discrimination of fetoplacental metabolism in normal and l-name-induced preeclamptic mice. *Metabolites.* 2021;11:376. doi:10.3390/metabo11060376
19. Markovic S, Roussel T, Agemy L, et al. Deuterium MRSI characterizations of glucose metabolism in orthotopic pancreatic cancer mouse models. *NMR Biomed.* 2021;34:1-12. doi:10.1002/nbm.4569
20. Mansfield P. Spatial mapping of the chemical shift in NMR. *Magn Reson Med.* 1984;1:370-386. doi:10.1002/mrm.1910010308
21. Posse S, Tedeschi G, Risinger R, Ogg R, Le Bihan D. High speed 1H spectroscopic imaging in human brain. *Magn Reson Med.* 1995;33:34-40.
22. Feinberg DA, Turner R, Jakab PD, Von Kienlin M. Echo-planar imaging with asymmetric gradient modulation and inner-volume excitation. *Magn Reson Med.* 1990;13:162-169. doi:10.1002/mrm.1910130116
23. Nam KM, Hendriks AD, Boer VO, Klomp DWJ, Wijnen JP, Bhogal A. Proton metabolic mapping of the brain at 7 T using a two-dimensional free induction decay–echo-planar spectroscopic imaging readout with lipid suppression. *NMR Biomed.* 2022;35:e4771.
24. Wilhelm T, Bachert P. In vivo 31 P echo-planar spectroscopic imaging of human calf muscle. *J Magn Reson.* 2001;149:126-130. doi:10.1006/jmre.2001.2288
25. Ulrich M, Wokrina T, Ende G, Lang M, Bachert P. 31P-{1H} echo-planar spectroscopic imaging of the human brain in vivo. *Magn Reson Med.* 2007;57:784-790. doi:10.1002/mrm.21192
26. Korzowski A, Bachert P. High-resolution 31P echo-planar spectroscopic imaging in vivo at 7T. *Magn Reson Med.* 2018;79:1251-1259. doi:10.1002/mrm.26785
27. Cunningham CH, Chen AP, Albers MJ, et al. Double spin-echo sequence for rapid spectroscopic imaging of hyperpolarized 13C. *J Magn Reson.* 2007;187:357-362. doi:10.1016/j.jmr.2007.05.014
28. Yen YF, Kohler SJ, Chen AP, et al. Imaging considerations for in vivo 13C metabolic mapping using hyperpolarized 13C-pyruvate. *Magn Reson Med.* 2009;62:1-10. doi:10.1002/mrm.21987
29. Larson PEZ, Hu S, Lustig M, et al. Fast dynamic 3D MR spectroscopic imaging with compressed sensing and multiband excitation pulses for hyperpolarized 13C studies. *Magn Reson Med.* 2011;65:610-619. doi:10.1002/mrm.22650
30. Mansfield P. Multi-planar image formation using NMR spin echoes. *J Phys C Solid State Phys.* 1977;10:L55-L58. doi:10.1088/0022-3719/10/3/004
31. Pohmann R, Von Kienlin M, Haase A. Theoretical evaluation and comparison of fast chemical shift imaging methods. *J Magn Reson.* 1997;129:145-160. doi:10.1006/jmre.1997.1245
32. de Graaf RA, Hendriks AD, Klomp DWJ, et al. On the magnetic field dependence of deuterium metabolic imaging. *NMR Biomed.* 2020;33:e4235. doi:10.1002/nbm.4235

33. De Feyter HM, de Graaf RA. Deuterium metabolic imaging—back to the future. *J Magn Reson.* 2021;326:106932. doi:10.1016/j.jmr.2021.106932
34. Gursan A, Hendriks A, Welting D, de Jong P, Klomp D, Prompers J. Deuterium body array for the simultaneous measurement of hepatic and renal glucose metabolism and gastric emptying with dynamic 3D deuterium metabolic imaging at 7T. *NMR Biomed*. 2023;e4926. doi:10.1002/nbm.4926
35. Schär M, Kozerke S, Fischer SE, Boesiger P. Cardiac SSFP imaging at 3 Tesla. *Magn Reson Med.* 2004;51:799-806. doi:10.1002/mrm.20024
36. Mareci TH, Brooker HR. High-resolution magnetic resonance spectra from a sensitive region defined with pulsed field gradients. *J Magn Reson.* 1984;57:157-163. doi:10.1016/0022-2364(84)90249-X
37. Pohmann R, Von Kienlin M. Accurate phosphorus metabolite images of the human heart by 3D acquisition-weighted CSI. *Magn Reson Med.* 2001;45:817-826. doi:10.1002/mrm.1110
38. Du W, Du YP, Fan X, Zamora MA, Karczmar GS. Reduction of spectral ghost artifacts in high-resolution echo-planar spectroscopic imaging of water and fat resonances. *Magn Reson Med.* 2003;49:1113-1120. doi:10.1002/mrm.10485
39. Roemer PB, Edelstein WA, Hayes CE, Souza SP, Mueller OM. The NMR phased array. *Magn Reson Med.* 1990;16:192-225. doi:10.1002/mrm.1910160203
40. Pruessmann KP, Weiger M, Scheidegger MB, Boesiger P. SENSE: sensitivity encoding for fast MRI. *Magn Reson Med.* 1999;42:952-962. doi:10.1002/(SICI)1522-2594(199911)42:5<952::AID-MRM16>3.0.CO;2-S
41. Kellman P, McVeigh ER. Image reconstruction in SNR units: a general method for SNR measurement. *Magn Reson Med.* 2005;54:1439-1447. doi:10.1002/mrm.20713
42. Brown MA. Time-domain combination of MR spectroscopy data acquired using phased-array coils. *Magn Reson Med.* 2004;52:1207-1213. doi:10.1002/mrm.20244
43. Dong Z, Peterson B. The rapid and automatic combination of proton MRSI data using multi-channel coils without water suppression. *Magn Reson Imaging.* 2007;25:1148-1154. doi:10.1016/j.mri.2007.01.005
44. Froeling M, Prompers JJ, Klomp DWJ, van der Velden TA. PCA denoising and wiener deconvolution of 31P 3D CSI data to enhance effective SNR and improve point spread function. *Magn Reson Med.* 2021;85:2992-3009. doi:10.1002/mrm.28654
45. Vanhamme L, Van Den Boogaart A, Van Huffel S. Improved method for accurate and efficient quantification of MRS data with use of prior knowledge. *J Magn Reson.* 1997;129:35-43. doi:10.1006/jmre.1997.1244
46. Purvis LAB, Clarke WT, Biasiolli L, Valkovič L, Robson MD, Rodgers CT. OXSA: an open-source magnetic resonance spectroscopy analysis toolbox in MATLAB. *PLoS One.* 2017;12:e0185356. doi:10.1371/journal.pone.0185356
47. Posse S, Tedeschi G, Risinger R, Ogg R, Le Bihan D. High speed 1H spectroscopic imaging in human brain by echo planar spatial-spectral encoding. *Magn Reson Med.* 1995;33:34-40. doi:10.1002/mrm.1910330106
48. de Graaf RA. *In Vivo NMR Spectroscopy: Principles and Techniques*. John Wiley & Sons; 2019. doi:10.1002/9781119382461
49. Otazo R, Mueller B, Ugurbil K, Wald L, Posse S. Signal-to-noise ratio and spectral linewidth improvements between 1.5 and 7 Tesla in proton echo-planar spectroscopic imaging. *Magn Reson Med.* 2006;56:1200-1210. doi:10.1002/mrm.21067
50. Versteeg E, van der Velden TA, van Leeuwen CC, et al. A plug-and-play, lightweight, single-axis gradient insert design for increasing spatiotemporal resolution in echo planar imaging-based brain imaging. *NMR Biomed.* 2021;34:1-13. doi:10.1002/nbm.4499
51. Versteeg E, Nam K, Klomp DW, et al. Silent EPSI using a gradient axis driven at 20 kHz. *Proceedings of the Annual Meeting of ISMRM & SMRT Virtual Conference & Exhibition, 08-14 August* 2020; Abstract #2908.
52. Liang Z-P. Spatiotemporal imaging with partially separable functions. *IEEE Int Symp Biomed Imaging.* 2007;2:988-991. doi:10.1109/ISBI.2007.357020
53. Korzowski A, Weinfurtner N, Mueller S, et al. Volumetric mapping of intra- and extracellular pH in the human brain using 31P MRSI at 7T. *Magn Reson Med.* 2020;84:1707-1723. doi:10.1002/mrm.28255
54. Lam F, Liang ZP. A subspace approach to high-resolution spectroscopic imaging. *Magn Reson Med.* 2014;71:1349-1357. doi:10.1002/mrm.25168
55. Lam F, Ma C, Clifford B, Johnson CL, Liang ZP. High-resolution 1H-MRSI of the brain using SPICE: data acquisition and image reconstruction. *Magn Reson Med.* 2016;76:1059-1070. doi:10.1002/mrm.26019
56. Zhao B, Lu W, Hitchens TK, Lam F, Ho C, Liang ZP. Accelerated MR parameter mapping with low-rank and sparsity constraints. *Magn Reson Med.* 2015;74:489-498. doi:10.1002/mrm.25421
57. Guo R, Zhao Y, Li Y, Li Y, Liang ZP. Simultaneous metabolic and functional imaging of the brain using SPICE. *Magn Reson Med.* 2019;82:1993-2002. doi:10.1002/mrm.27865
58. Haldar JP, Liang ZP. Spatiotemporal imaging with partially separable functions: a matrix recovery approach. *Proceedings of the 7th IEEE Int ernational Symposium on Biomedical Imaging: From Nano to Macro, Rotterdam, Netherlands*; April 2010:716-719. doi:10.1109/ISBI.2010.5490076
59. Ma C, Clifford B, Liu Y, et al. High-resolution dynamic 31P-MRSI using a low-rank tensor model. *Magn Reson Med.* 2017;78:419-428. doi:10.1002/mrm.26762
60. Nam KM, Gursan A, Lee NG, et al. 3D deuterium metabolic imaging of the human liver at 7T using low-rank and subspace modeling. *Proceedings of the Joint Annual Meeting of ISMRM-ESMRMB and ISMRT 31st Annual Meeting*, London, England, UK, 07-12 May 2022; Abstract #0632.
61. Bogner W, Otazo R, Henning A. Accelerated MR spectroscopic imaging—a review of current and emerging techniques. *NMR Biomed.* 2020;34:e4314. doi:10.1002/nbm.4314
62. Adalsteinsson E, Irarrazabal P, Topp S, Meyer C, Macovski A, Spielman DM. Volumetric spectroscopic imaging with spiral-based k-space trajectories. *Magn Reson Med.* 1998;39:889-898. doi:10.1002/mrm.1910390606
63. Furuyama JK, Wilson NE, Thomas MA. Spectroscopic imaging using concentrically circular echo-planar trajectories in vivo. *Magn Reson Med.* 2012;67:1515-1522. doi:10.1002/mrm.23184
64. Schirda CV, Tanase C, Boada FE. Rosette spectroscopic imaging: optimal parameters for alias-free, high sensitivity spectroscopic imaging. *J Magn Reson Imaging.* 2009;29:1375-1385. doi:10.1002/jmri.21760

65. Ramirez MS, Lee J, Walker CM, et al. Radial spectroscopic MRI of hyperpolarized [1-13C] pyruvate at 7 tesla. *Magn Reson Med.* 2014;72:986-995. doi:10.1002/mrm.25004
66. Saucedo A, Macey PM, Thomas MA. Accelerated radial echo-planar spectroscopic imaging using golden angle view-ordering and compressed-sensing reconstruction with total variation regularization. *Magn Reson Med.* 2021;86:46-61. doi:10.1002/mrm.28728
67. Gursan A, Froeling M, Hendriks AD, et al. Residual quadrupolar couplings observed in 7 tesla deuterium MR spectra of skeletal muscle. *Magn Reson Med.* 2022;87:1165-1173. doi:10.1002/mrm.29053

SUPPORTING INFORMATION

Additional supporting information may be found in the online version of the article at the publisher's website.

Figure S1. Three-dimensional data sets of the additional healthy volunteer at natural abundance, acquired with both deuterium Hamming–weighted MRSI (A) and echo-planar spectroscopic imaging (EPSI) acquisitions (B,C). The left panels show overlays of the ^{1}H-MRI images (Dixon) and the ^{2}H spectra. The liver is contoured in orange in the left panels. The right panels highlight the selected six voxels located in the liver (left panels, dark blue box), and the average SNR was calculated for 18 voxels from the three middle slices. Measurement parameters are the same as in Figure 3.

Figure S2. Temperature measurement of the gradients during two deuterium EPSI scans. Each EPSI scan was performed for about 10 min, and the interval between two EPSI scans was 47 min. The highest temperature was measured right after the EPSI scan was completed. After that, the temperature went down and stabilized after approximately 25 min. Note that the colors indicate different sensor positions on the gradient coil. The first three tracers (numbers 1, 2, and 3) are from sensors located on the shim coil, which are relatively less heated.

Figure S3. Deuterium spectra of the human brain at natural abundance, acquired with Hamming-weighted EPSI acquisition. (A) The T_1-weighted image is overlaid with the deuterium EPSI spectra. (B) Selected voxels in the posterior part of the brain (blue box) show the deuterium EPSI spectra. Water signals are present in the brain voxels and in voxels close to the skull, and lipid signals can be observed near the skull. Measurement parameters: voxel size = $20 \times 20 \times 20$ mm^3, FOV = 240 (AP) × 220 (RL) × 300 (FH) mm^3, TR/TE = 371/1.0 ms, FA = 90°, spectral bandwidth = 899 Hz, weighted averages = 12, number of time points = 256, and acquisition time = 3 min 41 s. AP, anterior–posterior; FA, flip angle; FH, feet–head; RL, right–left.

Figure S4. Deuterium spectra of the upper leg. (A) The T_1-weighted image is overlaid with the deuterium EPSI spectra. (B) Selected voxels in the leg (blue box) show the deuterium EPSI spectra. Naturally abundant deuterated water and lipid signals were visible in muscle and adipose tissue, respectively. The deuterated lipid signal was very sharp at all locations in the leg. The deuterated water signal in skeletal muscle was broadened (e.g., upper left voxels) or split (e.g., voxels in the lower row) due to residual deuterium quadrupolar couplings. The size of residual coupling depends on the angle between the muscle fibers and B_0.[67] Measurement parameters: voxel size = $20 \times 20 \times 20$ mm^3, FOV = 360 (RL) × 220 (AP) × 300 (FH) mm^3, TR/TE = 183/1.1 ms, FA = 60°, spectral bandwidth = 926 Hz, weighted averages = 42, number of time points = 64, and acquisition time = 9 min 55 s.

Table S1. SNR of natural abundance deuterated water signal in the human liver in vivo.

How to cite this article: Nam KM, Gursan A, Bhogal AA, et al. Deuterium echo-planar spectroscopic imaging (EPSI) in the human liver in vivo at 7 T. *Magn Reson Med*. 2023;90:863-874. doi: 10.1002/mrm.29696